Revision 2

Word count: 8099

High-pressure phase transition and equation of state of hydrous Al-bearing silica

Giacomo Criniti[1,*], Takayuki Ishii[2], Alexander Kurnosov[1], Konstantin Glazyrin[3], Tiziana Boffa Ballaran[1]

1 Bayerisches Geoinstitut, Universität Bayreuth, 95440 Bayreuth, Germany

2 Center for High Pressure Science and Technology Advanced Research, 100094 Beijing, China

3 Deutsches Elektronen-Synchrotron DESY, Notkestr. 85, 22603 Hamburg, Germany

* corresponding author: giacomo.criniti@uni-bayreuth.de

This is the peer-reviewed, final accepted version for American Mineralogist, published by the Mineralogical Society of America.
The published version is subject to change. Cite as Authors (Year) Title. American Mineralogist, in press.
DOI: https://doi.org/10.2138/am-2022-8546. http://www.minsocam.org/

Abstract

Stishovite, a rutile-structured polymorph of SiO_2, is a main component of subducted basaltic lithologies in the lower mantle. At mid lower-mantle depths, a second-order ferroelastic transition to orthorhombic $CaCl_2$-type (post-stishovite) structure occurs, causing extensive elastic shear softening. Previous studies showed that Al incorporation can decrease the transition pressure, while it is still debated whether H has a similar effect. Here we report the equations of state, structural evolution, and phase transformation of $Si_{0.948}Al_{0.052}O_{1.983}H_{0.018}$ (Al5) stishovite and $Si_{0.886}Al_{0.114}O_{1.980}H_{0.074}$ (Al11) post-stishovite samples using diamond anvil cells in combination with synchrotron X-ray diffraction and Raman spectroscopy. The Al5 sample transformed to the orthorhombic polymorph upon compression to 16 GPa, displaying a drop of ~12% in its bulk modulus across the transformation. The Al11 sample did not undergo any phase transition in the pressure range investigated. Single-crystal structural refinements and Raman spectroscopy measurements on the Al5 sample show that the soft optic mode B_{1g} is decoupled from the tetragonal-to-orthorhombic structural transformation and shows a plateau in the stability field of post-stishovite, between 20 and 30 GPa. This observation indicates that the transformation is not pseudo-proper ferroelastic as in SiO_2 stishovite and that existing Landau expansions are likely not applicable to H-rich Al-bearing silica samples. Using the equation of state parameters of orthorhombic Al5 and Al11 and literature data on SiO_2 post-stishovite we then discuss the possibility of non-ideal mixing along the SiO_2-AlOOH join.

Keywords: stishovite, X-ray diffraction, phase transition, equation of state, nominally anhydrous minerals

This is the peer-reviewed, final accepted version for American Mineralogist, published by the Mineralogical Society of America.
The published version is subject to change. Cite as Authors (Year) Title. American Mineralogist, in press.
DOI: https://doi.org/10.2138/am-2022-8546. http://www.minsocam.org/

Introduction

Stishovite is a high-pressure polymorph of SiO_2 with rutile-type structure (space group $P4_2/mnm$) that constitutes up to 25 vol.% of metabasaltic phase assemblages at lower mantle depths (e.g. Irifune & Ringwood, 1993; Ishii et al., 2019a, 2022). At about 50 GPa and room temperature, SiO_2 stishovite was found to undergo a second-order ferroelastic phase transition to a post-stishovite phase having $CaCl_2$-type structure (space group *Pnnm*), with a decrease from tetragonal to orthorhombic symmetry (Kingma et al. 1995; Andrault et al. 1998). Stishovite experiences extensive elastic softening across the post-stishovite transition, where its aggregate shear wave velocity (v_S) is expected to drop by about 20% (Carpenter et al. 2000). In the last few decades, seismological studies have detected a number of plate-like seismic scattering bodies having negative shear wave velocity anomalies ($-4\% < dv_S < -12\%$), but positive density anomalies ($+2\% < d\rho < +6\%$) compared to the surrounding mantle at about 1600-1800 km depth (e.g. Kaneshima & Helffrich, 1999; Niu, 2014). Temperature anomalies alone cannot explain such a drastic change in the elastic properties and density of the scatterers, which were therefore argued to represent chemically heterogeneous layers of dense subducted basalt (Kaneshima and Helffrich 1999). In addition, the shear elastic softening that characterizes the post-stishovite transition in subducted basalt matches well the elastic anomalies proposed for the scatterers (Kaneshima 2019), providing evidence for the recycling of subducted oceanic plates down to the mid-lower mantle.

More recently, scattering bodies displaying similar features have been detected in the proximity of subducted oceanic plates sinking or stagnating in the topmost lower mantle (Kaneshima 2019). These conditions are too shallow to be reconciled with the pressure and temperature conditions of the post-stishovite transition in SiO_2. In a dry mid-ocean ridge basalt (MORB) phase assemblage, however, stishovite is not pure SiO_2 and can host up to 4 mol% of $AlO_{1.5}$

component between 25 and 60 GPa (Ono et al. 2001; Hirose et al. 2005; Ricolleau et al. 2010; Ishii et al. 2019a, 2022). In the presence of water, the solubility of Al is even higher and reaches 7 mol% $AlO_{1.5}$ component, corresponding to about 6 wt.% Al_2O_3 (Litasov et al. 2007). It was shown that Al-enriched stishovite samples transformed to the post-stishovite phase at lower pressures compared to pure SiO_2 (Lakshtanov et al. 2005, 2007b; Bolfan-Casanova et al. 2009). In the previous study by Lakshtanov et al. (2007b), the soft optic (B_{1g}) and acoustic modes (v_S along the [110] direction) of a stishovite sample with composition $Al_{0.07}Si_{0.93}O_{1.97}H_{0.016}$ showed evidence for elastic softening around 25 GPa at room temperature. At the same pressure, splitting of Bragg reflections of the tetragonal phase was also observed, confirming that the sample had transformed to orthorhombic post-stishovite (Lakshtanov et al. 2007b). The amount of Al in stishovite necessary to reduce the transition pressure of the ferroelastic transition to be in accordance with the pressure at which the seismic scattering in the topmost lower mantle are observed is, however, much higher than determined in phase relations studies of hydrous MORB (Litasov and Ohtani 2005). More recent studies showed that also H-bearing Al-free stishovite exhibits lower transition pressure relative to SiO_2 (Nisr et al., 2017, 2020), suggesting that both Al and H can play a critical role in stabilizing the orthorhombic phase at lower pressures. Additionally, to date, the high-pressure structure and equation of state of hydrous Al-bearing stishovite and post-stishovite phases have been scarcely characterized, hampering our understanding of what are both individual and joint effects of H and Al on their elastic properties and transition mechanism and whether their combined presence may be a more likely explanation for the seismic scattering anomalies detected in the topmost lower mantle. For these reasons, in this study we report the high-pressure behavior of tetragonal $Si_{0.948}Al_{0.052}O_{1.983}H_{0.018}$ (Al5) and orthorhombic $Si_{0.886}Al_{0.114}O_{1.980}H_{0.074}$ (Al11) silica samples analyzed by means of single-crystal X-ray diffraction (XRD) and Raman spectroscopy in diamond anvil cell (DAC).

This is the peer-reviewed, final accepted version for American Mineralogist, published by the Mineralogical Society of America.
The published version is subject to change. Cite as Authors (Year) Title. American Mineralogist, in press.
DOI: https://doi.org/10.2138/am-2022-8546. http://www.minsocam.org/

Methods

Sample synthesis and characterization

Single crystals of hydrous Al-bearing silica were synthesized at high pressure and high temperature in the 15-MN Kawai-type multi-anvil apparatus with Osugi-type (DIA) guide block system installed at Bayerisches Geoinstitut, University of Bayreuth (Ishii et al. 2016, 2019b). The starting materials consisted of mixtures of SiO_2 and AlOOH-boehmite in molar ratios 95:5 (run I1072) and 8:2 (run I1063). Each mixture was ground in an agate mortar before being loaded in a Pt-tube capsule which was then sealed by welding. Tungsten carbide cubes with 3 mm truncated edge length were combined with a 7 mm Cr-doped MgO octahedral pressure medium and a $LaCrO_3$ heater. Temperature was monitored using a W97/Re3–W75/Re25 thermocouple. In both runs, the sample was first compressed to a target press load corresponding to 28 GPa (Liu et al. 2017) and then heated for 3-4 h at 1973 K (I1072) or 2173 K (I1063). Finally, the assembly was quenched by cutting the electrical power supply and slowly decompressed to ambient conditions.

The chemical composition of the run products was analyzed using a JEOL JXA-8200 electron probe microanalyzer (EPMA) operated at an acceleration voltage of 15 kV and a beam current of 5 nA using $MgSiO_3$ enstatite and Al_2O_3 corundum as standards for Si and Al, respectively. Chemical analysis revealed that the run products are chemically homogeneous throughout the entire length of each capsule based on the average of 15 data points per sample. The calculated oxide abundancies and estimated standard deviations (between parentheses) resulted to be SiO_2 = 94.32(56) wt.%, Al_2O_3 = 4.36(19) wt.% for I1072 and SiO_2 = 87.73(43) wt.%, Al_2O_3 = 9.54(14) wt.% for I1063. In order to quantify the water content of the two samples, inclusion-free single

crystals were hand-picked and polished on both sides to obtain platelets about 15 μm thick. Fourier transform infrared (FTIR) spectra were collected between 2000 and 10000 cm^{-1} with a spectral resolution of 4 cm^{-1} by averaging of 100-200 scans. In order to make a direct comparison with the sample of Lakshtanov et al. (2007b), H concentrations were determined using the calibration of Paterson (1982). Unpolarized FTIR measurements were conducted on randomly oriented crystals for run I1063, while polarized FTIR measurements were performed on the (100) crystallographic plane of a single crystal from run I1072. Although the FTIR measurements were conducted on different crystals than those employed in high-pressure experiments, we expect that the water concentration is homogeneous in the run products, similarly to what we found for the Al and Si content in our EPMA analyses. We found that water contents of I1063 and I1072 samples were 1.1(5) wt.% and 0.27(8) wt.%, respectively, where the numbers between parentheses represent either the standard deviation calculated from different unpolarized measurements (I1063) or the effect of using different baseline subtraction strategies (I1072). Further details about the analytical procedure and water content determination will be reported in a separate publication. The overall compositions of the two samples resulted to be $Si_{0.886(4)}Al_{0.114(2)}O_{1.980}H_{0.07(3)}$ (Al11) and $Si_{0.948(6)}Al_{0.052(2)}O_{1.983}H_{0.018(5)}$ (Al5). Preliminary in-house single-crystal X-ray diffraction (XRD) measurements were performed on a Huber diffractometer equipped with Mo$K\alpha$ radiation and a point detector and driven by the software SINGLE (Angel and Finger 2011). Al5 displayed tetragonal symmetry, like Al-rich stishovite samples reported in a previous study (Litasov et al. 2007), with unit-cell lattice parameters a = 4.1988(1) Å, c = 2.6730(1) Å and V = 47.125(3) $Å^3$. Al11, on the other hand, exhibited the high-pressure orthorhombic $CaCl_2$-type structure of post-stishovite, with unit-cell lattice parameters a = 4.2597(2) Å, b = 4.1831(4) Å, c = 2.6829(1) Å and V = 47.806(6) $Å^3$.

High-pressure X-ray diffraction measurements

Single crystals of Al5 (15x15x10 μm^3) and Al11 (20x10x10 μm^3) were loaded in a BX90-type DAC (Kantor et al. 2012) equipped with Almax-Boehler diamonds (Boehler and De Hantsetters 2004) having culets of 350 μm in diameter (Supplementary Table S1). A 200 μm-thick Re foil was indented to 51(1) μm and drilled using an infrared laser to obtain the sample chamber. The Al5 and Al11 samples were loaded in the same sample chamber together with a ruby sphere for pressure determination (Shen et al. 2020) and a piece of Au. Pre-compressed He gas at 1.3 kbar was loaded as quasi-hydrostatic pressure transmitting medium using the gas loading system installed at the Bayerishces Geoinstitut, University of Bayreuth (Kurnosov et al., 2007).

High-pressure XRD measurements were conducted at the Extreme Conditions Beamline P02.2 of PETRA III (DESY, Hamburg, Germany) using a 2 x 2 μm^2 X-ray beam of 42.7 keV and a Perkin-Elmer XRD 1621 flat panel detector (Liermann et al. 2015). Polycrystalline CeO_2 and a single crystal of natural enstatite were measured to calibrate the sample-detector distance and instrument parameters for single-crystal XRD, respectively. Pressure was increased online using a gas-driven membrane up to ~50 GPa at steps of 1-2 GPa. As it is commonly observed for ferroelastic phase transitions (e.g. Salje 1991), twin structures develop in hydrous Al-bearing stishovite upon transformation to the $CaCl_2$-type phase (Lakshtanov et al. 2007b), where the twin law consist of a reflection of the two lattices by the {110} planes. The Al11 sample displayed the same type of twinning already at ambient conditions, suggesting that the same type of twinning may occur as well during crystal growth in the stability field of the $CaCl_2$-type phase. The Al5 sample was not twinned at ambient conditions, but ferroelastic twin domains developed at the onset of the phase transition to $CaCl_2$-type phase. In the proximity of the phase transition, when the orientations of the twin components are too close to each other, peaks at low 2θ values are difficult to distinguish in single-crystal diffraction step scans. Although this problem was observed only in the Al5 sample and only in a limited pressure range, we decided to determine

the unit-cell parameters of both Al5 and Al11 (Supplementary Tables S2 and S3) by fitting 1D profiles to avoid systematic differences that could arise due to the proximity and/or overlapping of reflections between the two twin components at different pressures. For this purpose, wide-scan images were collected upon continuous rotation of the DAC between -20° and +20° and integrated to 1D patterns using DIOPTAS (Prescher and Prakapenka 2015). Full profile Le Bail fits were then obtained using *JANA2006* (Petrícek et al. 2014).

Step scans were also acquired at each pressure point upon continuous rotation of the DAC between -35° and +35° and processed using CrisAlysPro (Agilent Technologies Ltd., Yarton, Oxfordshire, UK). Data processing included peak search and indexing, background subtraction, intensity integration, Lorentz and polarization corrections, frame scaling and empirical absorption correction based on spherical harmonics. For the Al11 sample, the orientation matrices of the two twin components were sufficiently different from each other. Therefore, the intensity data from the two twin domains were simultaneously integrated and then merged in a single reflection file that was used for structural refinements. For the Al5 sample, this strategy could not be applied in the proximity of the phase transformation where the reflections of the two twin components were too close to each other at low 2θ angles. For internal consistence, we decided instead to use a small mask and integrate only the most intense of the two domains at all pressure points, excluding reflections that would overlap with the other twin component. A comparison of the two integration strategies for the Al5 sample at the highest pressures, where the orientations of the two twin components were sufficiently different, yielded very consistent results, with structural parameters being almost identical within their mutual uncertainties, confirming the robustness of our approach. The structures of the two phases were solved using the dual space algorithm *SHELXT* (Sheldrick 2015b) and refinements against F^2 were performed with *SHELXL* in the *Shelxle* GUI (Hübschle et al. 2011; Sheldrick 2015a). Atomic scattering

factors were used in all refinements and site occupancies at the cation site were fixed to Si = 0.95 and Al = 0.05 for Al5 and Si = 0.89 and Al = 0.11 for Al11, as determined from chemical analyses. The hydrogen atoms could not be located in the structure because of their low concentration and extremely weak scattering factor. Anisotropic displacement parameters were employed for all atoms, except for data collected at 21.75(3) and 32.21(4) GPa on Al5, where isotropic parameters were used due to the lower number of observed reflections. *R*-factors obtained for structural refinements were typically between 3% and 5% for both samples, proving the high quality of our structural models. Further information can be found in the deposited Crystallographic Information File (CIF).

High-pressure Raman spectroscopy

Two crystals with Al5 and Al11 compositions were further analyzed at high-pressure and room temperature in DACs by means of Raman spectroscopy. Several runs were performed employing BX-90 DACs with Almax-Boehler diamonds having culet diameters of 400 or 250 μm, Re as gasket material and He or Ne as pressure transmitting media (Supplementary Table S1). A ruby sphere was loaded in each DAC as pressure standard (Shen et al. 2020). Pressure was increased manually by mechanically tightening the screws of the DACs up to about 40 or 44 GPa at steps of 0.5 - 3 GPa. Raman spectroscopy measurements were performed on a Dilor XY Spectrometer equipped with a 50x microscope objective and a 1800 groove/mm diffraction grating. The spectrometer employed a 532 nm ventus532 laser from Laser Quantum and a TE cooled SynapseTM CCD detector (1024x256 resolution) from HORIBA Jobin Yvon, and was driven by LABRAM 5 software. Raman spectra were acquired using a laser power of 200-800 mW between 150 and 500 cm^{-1} with a resolution of 2 cm^{-1}. To analyze the high-pressure Raman spectra of Al5 and Al11 samples, background was manually subtracted from each spectrum and peaks were fitted using pseudo-Voigt functions using the software package Origin 2019

(OriginLab corporation, Northampton, MA, USA). The peak positions of the Raman optic mode and their estimated standard deviations for Al5 and Al11 samples are reported as supplementary material (Supplementary Tables S4 and S5).

Results and discussion

Equation of state of hydrous Al-bearing silica

The pressure evolution of the unit-cell parameters of Al5 and Al11 samples is shown in Figure 1. The Al5 sample retained its tetragonal symmetry up to 13.83(3) GPa, after which transformed to the orthorhombic $CaCl_2$-type phase, as observed by the divergence of the *a* and *b* unit-cell parameters (Figure 1b). The Al11 sample exhibited the $CaCl_2$-type structure of post-stishovite already at ambient conditions, suggesting that such structural modification is quenchable as long as a sufficient amount of Al and H is present in the stishovite crystal structure. The orthorhombic symmetry of Al11 was retained upon compression to 50.13(4) GPa and no phase transformations were detected in the pressure range investigated. EOSFit7c in the EOSFit GUI software (Angel et al., 2014; Gonzalez-Platas et al., 2016) was used to fit 3rd-order Birch-Murnaghan (BM3) equations of state (EOS) to our *P*-*V* datasets (Angel et al., 2014; Birch, 1947):

$$P = \frac{3}{2}K_{T0}\left[\left(\frac{V_0}{V}\right)^{\frac{7}{3}} - \left(\frac{V_0}{V}\right)^{\frac{5}{3}}\right]\left\{1 + \frac{3}{4}(K'_{T0} - 4)\left[\left(\frac{V_0}{V}\right)^{\frac{2}{3}} - 1\right]\right\} \quad \#(1)$$

Where V_0 is the ambient pressure unit-cell volume, K_{T0} the isothermal bulk modulus at ambient conditions and K'_{T0} is its pressure derivative. Due to the limited pressure interval in which the tetragonal polymorph of Al5 is stable, its K'_{T0} was fixed to 4.8, as reported by Zhang et al. (2021) for SiO_2 stishovite based on single-crystal XRD measurements. The refined EOS parameters are consistent with the analysis of the F-f_E plots of both samples, as shown in the supplementary

This is the peer-reviewed, final accepted version for American Mineralogist, published by the Mineralogical Society of America.
The published version is subject to change. Cite as Authors (Year) Title. American Mineralogist, in press.
DOI: https://doi.org/10.2138/am-2022-8546. http://www.minsocam.org/

material (Supplementary Figure S1). Static compression and elasticity measurements on SiO_2 reported, on average, a bulk modulus of 310 GPa for stishovite at ambient conditions (Weidner et al. 1982; Andrault et al. 2003; Jiang et al. 2009; Zhang et al. 2021). The K_{T0} value of our tetragonal sample Al5, i.e. 299(2) GPa, is smaller than that of SiO_2 stishovite, but larger than that of other Al-bearing samples investigated in previous studies (Figure 2). $AlO_{1.5}$ incorporation in dry stishovite (Bolfan-Casanova et al., 2009) seems to induce a more pronounced reduction of the bulk modulus than that observed for Al,H-bearing samples (Figure 2), possibly due to higher concentration of oxygen vacancies related to the substitution of the $AlO_{1.5}$ component. H-poor Al-bearing stishovite samples were also previously analyzed by Brillouin scattering (Lakshtanov et al. 2007a), showing values of the adiabatic bulk modulus, K_{S0}, similar to those of K_{T0} determined in our study (Figure 2). Since K_{S0} at ambient conditions is usually only 1-2% larger than K_{T0}, the data of Lakshtanov et al. (2007a) support the observation that increasing the H content for a given Al concentration in stishovite increases the bulk modulus. At pressure higher than 16 GPa, after the tetragonal to orthorhombic transition in Al5, K_T of the sample decreases by ~12% and becomes identical to that of Al11 within uncertainty (Supplementary Figure S2), albeit with a slightly steeper slope due to its larger K'_{T0} (Table 1).

Axial compressibility of hydrous Al-bearing silica

Following the approach of Angel (2000) and Angel et al. (2014), we used a linearized BM3 EOS to describe the pressure evolution of the unit-cell parameters (l) by substituting V with l^3, $3K_{T0}$ with $M_{l,0}$ and $3K'_{T0}$ with $M'_{l,0}$:

$$P = \frac{1}{2} M_{l,0} \left[\left(\frac{l_0}{l}\right)^7 - \left(\frac{l_0}{l}\right)^5 \right] \left\{ 1 + \frac{1}{4}\left(M'_{l,0} - 12\right) \left[\left(\frac{l_0}{l}\right)^2 - 1 \right] \right\} \quad \#(2)$$

Due to the little sensitivity of our dataset to the $M'_{c,0}$ of Al5, its value was fixed to 0 in the tetragonal phase (i.e. the compression of the c-axis was assumed to be linear up to 16 GPa) and

to 1.3 in the orthorhombic phase, the latter of which is the value determined for the Al11 sample, given that the evolution with pressure of the orthorhombic *c*-axis seems identical for the two samples. A complete list of the refined EOS parameters is provided in Table 1. The *c*-axis is the most incompressible direction in both samples and seems to be not much affected by changes in the chemical composition and crystal structure of hydrous Al-bearing SiO_2. By comparing the linear equations of state of tetragonal and orthorhombic Al5, only a very subtle softening of the *c*-axis was detected across the phase transition (Figure 1c), consistently with previous observations on SiO_2 stishovite (e.g. Andrault et al., 2003). The *a* and *b* lattice parameters of Al5 quickly diverged upon transformation to the $CaCl_2$-type phase (Figure 1b), although their EOSs became practically subparallel to those of Al11 at about 50 GPa. The resulting axial compressibility for tetragonal Al5 and for orthorhombic Al5 and Al11 followed the schemes $\beta_a > \beta_c$ and $\beta_b > \beta_a > \beta_c$, respectively.

Spontaneous strains and structural distortion analysis

In a ferroelastic transition, such as that of SiO_2 stishovite, the pressure evolution of the spontaneous strains in the low-symmetry orthorhombic phase (i.e. the fractional change in the unit-cell parameters relative to the high-symmetry phase) yields important information about the anisotropic elastic properties of that material (Carpenter et al. 2000; Buchen et al. 2018; Zhang et al. 2021). In the particular case of stishovite, these strains can be defined as $e_1 = (a\text{-}a_t)/a_t$ and $e_2 = (b\text{-}a_t)/a_t$ where *a* and *b* are unit-cell lattice parameters of the low-symmetry $CaCl_2$-type phase at a given pressure and a_t is the *a* lattice parameter that the high-symmetry phase would have at the same pressure. When the phase transition to the low-symmetry orthorhombic phase occurs, *a* and *b* become free to vary and diverge from the value that they would have in the high-symmetry tetragonal phase. A symmetry breaking strain that quantifies the distortion of the low-symmetry

phase relative to the high-symmetry phase can then be defined as the difference between e_1 and e_2.

Spontaneous strains and elastic properties of a material can be related to each other using a Landau free energy expansion of the order parameter Q driving a phase transition (Carpenter et al. 1998). The order parameter is in general represented by the magnitude or amplitude of a given structural feature (e.g., atomic displacement, tilt angle, etc.). Q is, by definition, zero in the high-symmetry phase and free to vary in the low-symmetry phase. The transformation of SiO_2 stishovite to $CaCl_2$-type phase is a pseudo-proper ferroelastic one, where the order parameter Q can be described in terms of the octahedral tilting (as discussed in detail in the next paragraph) and is related to the soft optic mode of stishovite (Carpenter et al. 2000). Moreover, Q couples linearly with the symmetry-breaking strain, causing a violation of the Born stability criterion $c_{11} - c_{12} > 0$, which approaches zero in the proximity of the phase transformation and causes elastic instability and shear softening along the [110] direction (Carpenter et al., 2000). For Al5, the values of e_1 and e_2 were calculated according to the relations reported above from the measured unit-cell lattice parameters of the low-symmetry phase at a given pressure and the unit-cell lattice parameters of the high-symmetry phase extrapolated to the same pressure using the linear EOS parameters reported in Table 1. When $(e_1 - e_2)^2$ is plotted against pressure for SiO_2 stishovite, a linear fit of the squared symmetry breaking strain yields the transition pressure (P_c^*), at which elastic softening is most extensive (Carpenter et al., 2000). Spontaneous strains calculated for Al5 (Figure 3), however, show a concave trend up to 35 GPa. A linear fit of the data was only possible above this pressure and yielded $P_c^* = 24.7(1.1)$ GPa, which is much higher than the observed transition pressure of about 16 GPa for the tetragonal-to-orthorhombic transition.

Further insights on the nature of the phase transition of Al5 may be obtained by considering the relationship between the crystal structures of Al-bearing stishovite and post-stishovite.

290 According to group theory, the space group of post-stishovite (*Pnnm*) has the same symmetry
291 elements as the space group of stishovite ($P4_2/mnm$) apart from the 4-fold symmetry axis.
292 Therefore, *Pnnm* is called a subgroup of $P4_2/mnm$. Note, however, that the differences between
293 the *Pnnm* and $P4_2/mnm$ structures of silica are not only in the point group symmetry, which
294 affects the length of the *a* and *b* unit-cell edges, but also in the position of atoms in the unit-cells
295 of the two phases. In the case of stishovite, the point symmetry at the oxygen position across the
296 $P4_2/mnm$ to *Pnnm* transition changes from m.2m (x,-x,0) to ..m (x,y,0) and therefore acquires one
297 degree of freedom. As a result, the *y* fractional coordinate of oxygen in the orthorhombic phase
298 (Supplementary Table S6) deviates from the value that it would have in the tetragonal phase (i.e.
299 -x), causing the SiO_6 octahedra in the *a*-*b* plane of the orthorhombic phase to rotate giving rise to
300 octahedral tilting. In Figure 4, the pressure evolution of the octahedral tilting angles (η) is shown
301 for the Al5 and Al11 samples. In the Al5 sample, this angle is 90° due to symmetry constraints in
302 the tetragonal phase and deviates from such value after transformation to the orthorhombic
303 phase. The evolution of η with pressure becomes linear above 25 GPa. The octahedral tilting in
304 the Al11 sample, on the other hand, shows a linear trend throughout the entire pressure range
305 investigated (Figure 4). Note that even at room pressure the η angles for Al11 samples are very
306 different from 90°, suggesting that the Al and H substitution affects primarily the octahedral
307 tilting, stabilizing in this way the orthorhombic structure. Another way for quantifying the
308 octahedral tilting is by using the irreducible representation (irrep) Γ2+ of the space group
309 $P4_2/mnm$ (Miller and Love 1967) describing the displacement of the oxygen from the (x,x,0)
310 position. Γ2+ coincides with the order parameter *Q* and has the same point group symmetry as
311 the optic soft mode B_{1g} of the stishovite structure. In SiO_2 stishovite, the tilting of the SiO_6
312 octahedra is coupled with the soft optic mode B_{1g} in the tetragonal phase and is responsible for
313 the elastic softening that has been observed in the [110] direction prior to and across the phase

transition (Zhang et al. 2021). In order to determine the variation of Γ2+ and thus quantify the order parameter variation as a function of pressure, a symmetry-mode decomposition analysis for the Al5 sample was performed using the computer program AMPLIMODES (Orobengoa et al. 2009). The input files required for calculating the amplitude of the irrep Γ2+ are the unit-cell parameters and atomic coordinate of the high- and low-symmetry phases at the same pressure conditions. As far as the orthorhombic phase is concerned, these quantities were directly derived from the analysis of diffraction patterns and single-crystal structural refinements, as described above. For the high-symmetry phase, on the other hand, the unit-cell parameters and the atomic coordinates of the Si and O sites needed to be extrapolated to the pressure range where the orthorhombic phase is stable. The unit-cell parameters of the tetragonal phase above 16 GPa were easily obtained by extrapolating the linear EOS (Equation 2) of the *a* and *c* lattice parameters determined below 16 GPa (Supplementary Table S2). The *x* atomic coordinate of the O atom, on the other hand, was found to be basically pressure-independent between 0 and 16 GPa, having an average value of 0.3054 (Supplementary Figure S3, Supplementary Table S6) and therefore this values well describe the tetragonal oxygen position at all pressures. The position of Si is (0,0,0) in both phases. When the angle (η - 90°) and of the symmetry breaking strain (e_1 - e_2) are plotted against Γ2+, a linear relationship is found (Figure 5) as expected for the coupling between order parameter and spontaneous strain for a tetragonal ($P4_2/mnm$) to orthorhombic ($Pnnm$) transition. Given these relationships, also the evolution of $\Gamma 2+^2$ vs P was found to be concave in the proximity of the phase transition, similarly to the case of the symmetry breaking strain, and a linear fit of the $\Gamma 2+^2$ data is only possible above 35 GPa (Figure 3). The resulting transition pressure would be $P_c^* = 24.1(1.9)$ GPa, which is consistent with the value obtained from the fit of $(e_1 - e_2)^2$ but much larger than the effective transition pressure observed by XRD.

This is the peer-reviewed, final accepted version for American Mineralogist, published by the Mineralogical Society of America.
The published version is subject to change. Cite as Authors (Year) Title. American Mineralogist, in press.
DOI: https://doi.org/10.2138/am-2022-8546. http://www.minsocam.org/

High-pressure evolution of the optic soft mode

The low wavenumber region of Raman spectra, where the B_{1g} (tetragonal structure) and A_g (orthorhombic structure) lattice modes (Supplementary Tables S4 and S5) can be observed, is shown for Al5 (180 ~ 250 cm^{-1}) and Al11 (180 ~ 330 cm^{-1}) in Figure 6a and 6b, respectively. By analyzing the full width at half maximum (FWHM) of the measured Raman peaks, we observed that the peak widths remained almost constant between 0 and 20 GPa (FWHM ~ 6 cm^{-1}) for data collected for Al5, while slight broadening was detected between 20 and 30 GPa for Al5 (FWHM ~ 8 cm^{-1}) and between 0 and 25 GPa for Al11 (FWHM ~ 8-14 cm^{-1}), where the Raman shifts of the optic modes of the two samples seem to be pressure-independent (Figure 6c). Further broadening of the peaks occurred above 30 GPa for Al5 and above 25 GPa for Al11, where the Raman signals could be fitted as a doublet peak. Note that, for Al5, the intensity of the peak at lower wavenumber progressively decreased at higher pressures and it is only a small shoulder at 38 GPa (Figure 6a). A similar behavior was observed for Al11 above 25 GPa (Figure 6b). At first, a small shoulder appeared at higher wavenumber to the main peak, then it rapidly evolved into a doublet of peaks having similar intensity, with the linewidth of the peak at higher wavenumber being about 1.5-2 times larger than that of the peak at lower wavenumber. Within a few GPa interval, the intensity of the peak at higher wavenumber rapidly increased while the peak at lower wavenumber disappeared (Figure 6b, Supplementary Figure S4). Peak splitting across the post-stishovite transformation was previously reported for SiO_2 stishovite upon compression under non-hydrostatic conditions (Kingma et al., 1995), but was not visible in a more recent study where Ne was employed as pressure transmitting medium (Zhang et al., 2021). In this study, Raman spectroscopy measurements at the highest pressures were conducted using He as pressure transmitting medium (Supplementary Table S1), which is known to provide an even more hydrostatic environment than Ne in the pressure interval investigated in this study. In

addition, single crystals used for Raman spectroscopy measurements were as thin as 10 μm. Therefore, we exclude that the observed splitting of the Raman peaks of Al5 and Al11 at pressures higher than 25 GPa is related to non-hydrostatic conditions in our DACs or bridging between diamond anvils and the samples. Moreover, in the case of Al11, the shoulder completely disappeared at higher pressure without thermally annealing the sample (Figure 6b, Supplementary Figure S4). We therefore suggest that the presence of two peaks in the Raman spectra is due to fluctuations of the order parameter associated with octahedral tilting. i.e. by differences in the magnitude of the order parameter between adjacent unit-cells due to their different crystal or defect chemistry. Fluctuations are invisible to XRD techniques, which provide information only on the long-range order of the crystal structure, while Raman spectroscopy probes interactions taking place at a much shorter scale and therefore is sensitive to the different local environments arising from the substitution of Si^{4+} by Al^{3+} and H^{+} or from the presence of oxygen vacancies. Since Al and H occupy only a relatively small number of unit-cells (i.e. 10% in Al5 and 22% in Al11), we can expect a distribution of unit-cells displaying different tilting at the local scale. According to our interpretation, the peak at higher wavenumber would represent more distorted environments, where the structure is more affected by the substitution of Si by Al and H, while the shoulder or peak at lower wavenumber indicates regions of the sample with a smaller degree of distortion.

Following Carpenter et al. (2000), the square of wavenumber (ω^2) of the soft optic mode of tetragonal stishovite (B_{1g}) as well as that of the A_g optic mode of orthorhombic post-stishovite have been plotted as a function of pressure for Al5 and Al11 (Figure 6c). In the figure, we have reported only the peak at higher wavenumber because (i) it was the most intense peak at the highest pressures and (ii) it was the dominant feature in the Raman spectra collected upon decompression (Figure 6a,b). It is known that some fluctuations are time-dependent and the

disappearance of the shoulder with increasing pressure further supports the fluctuations hypothesis. As expected, ω^2 decreases linearly for the high-symmetry phase of Al5, as observed for pure SiO_2-stishovite (Kingma et al. 1995; Zhang et al. 2021) and poorly hydrated Al-bearing stishovite (Lakshtanov et al. 2007b) (Figure 6c). However, after the transformation of Al5 to orthorhombic symmetry above 16 GPa, the optic mode continues to decrease following the same trend up to ~20 GPa, then flattens and stays constant up to ~30 GPa. Only above 30 GPa, the Raman shifts starts to increase with a slope similar in magnitude to that shown by the decreasing B_{1g} mode (Figure 6c). For Al11, a similar plateau in the high-pressure evolution of ω^2 for the optic mode A_g is observed between 0 and 25 GPa (Figure 6c), despite the sample showed no evidence of structural phase transition in the investigate pressure range. Above this pressure, ω^2 increases linearly with a steeper slope than that shown by Al5 above 30 GPa.

Effect of H on the post-stishovite transition mechanism

From the combination of XRD, structural and Raman spectroscopy data, it is evident that the tetragonal-to-orthorhombic transition observed in Al5 at ~16 GPa and the optic mode plateau between 20 and 30 GPa result from a different transformation mechanism than that of the ferroelastic transition of SiO_2 and H-poor Al-bearing stishovite. While it appears that a higher H content than reported by Laksthanov et al. (2007b) can further reduce the transition pressure of Al-bearing stishovite, the decoupling of the structural phase transition from the soft optic mode behavior prevents us from making a more quantitative comparison with samples investigated in previous studies. In the compounds studied so far in the literature, in fact, the splitting of Bragg reflections denoting the transition to the orthorhombic structure was observed at the same pressure where the trends of soft optic mode, as well as those of the soft acoustic mode, for the high-symmetry and low-symmetry phases met (e.g., Lakshtanov et al. 2007b; Zhang et al. 2021). The decoupling between the order parameter and the soft optic mode observed in this study

prevents us from applying published Landau expansions for the ferroelastic transition of SiO_2 to our Al5 sample. One possible explanation for the observed behavior could lie in the different Al/H ratios of Al-bearing silica samples investigated here (Al/H ~ 2) and in the previous study of Lakshtanov et al. (2007b) (Al/H ~ 4). The XRD data collected for Al5 do not allow to refine the H position in this sample, due to the fact that only ~ 0.02 hydrogen atoms per formula unit are present. Given the strong anisotropy of polarized FTIR spectra observed in hydrous Al-bearing stishovite (Pawley et al. 1993; Litasov et al. 2007; Thomas et al. 2009), the O-H vectors have been proposed to lie perpendicular to the *c*-axis. Based on neutron diffraction measurements on isostructural H-bearing rutile, Smith et al. (1995) proposed that H atoms in stishovite have fractional coordinates (0.5,0.42,0). The related O···O vectors, however, measure about 2.3 Å in Al-bearing silica and constitute the shortest intra-octahedral distances, corresponding to the shared edge of $(Si,Al)O_6$ octahedra perpendicular to the *c*-axis. More recent first principle calculations suggested that H atoms are bonded either to the apical (H1) or the equatorial (H2) oxygens of the octahedra that host the Al impurities, with O-H vectors actually pointing towards the empty channels of the stishovite structure (Umemoto et al. 2016). The H1 position, located in the proximity of (0.5,0,0), corresponds to the position of hydrogen in δ-AlOOH (Sano-Furukawa et al. 2018) and was found to be energetically more stable than H2 (Umemoto et al. 2016). Therefore, we argue that H atoms in the hydrous Al-bearing samples analyzed in this study are incorporated as in the isostructural compound δ-AlOOH. In this scenario, the strain field induced by H incorporation in the structure of Al-bearing silica propagates at the local scale through the displacements of O atoms towards or away from H, causing a tilt of $(Si,Al)O_6$ octahedral units. If the concentration of oxygen vacancies is large enough, H atoms might not "see" each other's strain fields as some of the O atoms through which the strain field propagates are actually missing. As a consequence, the effect of H on the post-stishovite transition might be negligible in

samples with a sufficiently large Al/H ratio and the transition mechanism would result similar to that of SiO_2 stishovite (Lakshtanov et al. 2007b). The delayed response of the soft optic mode to the post-stishovite transition and the plateau of the vibrational frequencies observed in our samples would suggest that there may be two different transformations, both involving the tilting of octahedra, that take place in a relatively narrow pressure interval. Despite never being observed in stishovite samples before, a plateau of the vibrational frequencies in ferroic materials is in fact not unusual. For instance, recent resonant ultrasound spectroscopy (RUS) measurements of Co-doped Fe-pnictide at low temperature highlighted similar features, which were explained as the effect of interacting parameters driving different structural transition in a narrow temperature interval (Carpenter et al. 2019). In the light of all the above-mentioned considerations, the post-stishovite transition in H-rich Al-bearing silica cannot be regarded as a pure second-order ferroelastic transformation and further measurements of its elasticity and H-bond evolution at high pressure are required to quantitatively constrain the extent of its elastic shear softening and the involved transformation mechanism.

If the observed decoupling of optic mode and structural phase transitions arises from the interaction of two order parameters related to different phase transformation, a similar behavior may be expected for H-bearing davemaoite, i.e., $CaSiO_3$ with perovskite structure. This mineral is expected to undergo a second-order ferroelastic transition from tetragonal to cubic symmetry with increasing temperature driven by octahedral tilting (e.g., Komabayashi et al. 2007; Stixrude et al. 2007). Additionally, recent in-situ IR measurements showed that the O-H stretching frequency of H-bearing $CaSiO_3$ davemaoite decreases with increasing pressure, suggesting that a H-bond symmetrization may occur at pressures of the lower mantle (Chen et al. 2020). Further investigations on the H-bond evolution and transition mechanism of H-bearing $CaSiO_3$

This is the peer-reviewed, final accepted version for American Mineralogist, published by the Mineralogical Society of America.
The published version is subject to change. Cite as Authors (Year) Title. American Mineralogist, in press.
DOI: https://doi.org/10.2138/am-2022-8546. http://www.minsocam.org/

davemaoite may also help to understand whether the behavior observed in this study is unique to stishovite or is shared with other lower mantle mineral phases.

Implications

As discussed above, the decoupling between the soft optic mode and the structural phase transition of hydrous Al-bearing stishovite can affect the pressure interval where elastic softening associated with the ferroelastic transition occurs. The Clapeyron slope of the post stishovite transition is positive (e.g. Nomura et al. 2010; Fischer et al. 2018), meaning that the transition pressure increases with increasing temperature. We can think of two possible scenarios where the soft acoustic mode (i.e. the v_S of stishovite along the [110] direction) would be coupled either with the soft optic mode or with the octahedral tilting. In the former case, elastic softening at room temperature would be observed in the pressure range of the plateau region of the soft optic mode (i.e., around 20-30 GPa) which overlaps with the transition pressure of about 25 GPa reported by Lakshtanov et al. (2007b). Extrapolation to subducting slab temperatures (Kirby et al. 1996; Eberle et al. 2002) would move the boundary up by about 10 GPa (Nomura et al. 2010) corresponding to the pressure range where seismic scattering anomalies have been located by seismological methods in the proximity of subducting slabs (Kaneshima 2019). In the latter case, acoustic softening would be observed in the proximity of the structural transformation (i.e., around 16 GPa) at room temperature and extrapolation to high temperature would yield a transition pressure corresponding to the very top portion of the lower mantle, where only few seismic scatterers have been observed so far. Based on our results and on previous observations, we have suggested that not only the H content but also the Al/H ratio is a critical factor in lowering the transition pressure of hydrous Al-bearing stishovite to post-stishovite. Therefore, negative dv_S anomalies associated with seismic scattering could be explained by the presence of

481 hydrous stishovite with lower Al contents than our samples, but with similar or even lower Al/H
482 ratios, thus closer to the SiO_2-AlOOH join. Slightly lower Al content would then be in good
483 agreement with previous experimental phase relations studies at topmost lower mantle conditions
484 (Ono et al. 2001; Litasov and Ohtani 2005; Ishii et al. 2019b, 2022). Further elasticity
485 measurements across the structural phase transformation of hydrous Al-bearing silica will allow
486 to pinpoint the pressure range and the extent of its elastic shear softening, enabling us to evaluate
487 its actual geophysical relevance.

488 Accurate EOS parameters for hydrous Al-bearing silica are also important to understand the
489 seismic signature of Al-bearing post-stishovite and its solid solution behavior with $CaCl_2$-type δ-
490 AlOOH. In Figure 7, we compare the high-pressure evolution of K_T of our samples with those of
491 isostructural SiO_2 and AlOOH obtained in previous studies by isothermal compression and
492 elasticity measurements (Andrault et al. 2003; Sano-Furukawa et al. 2009; Buchen et al. 2018;
493 Fischer et al. 2018; Zhang et al. 2021). There is clearly a large variation in the K_T behaviour
494 among the different studies. However, when we compare our data with measurements performed
495 under quasi-hydrostatic conditions (i.e., Zhang et al. (2021) for post-stishovite and δ-AlOOH
496 (Sano-Furukawa et al. (2009), the K_T curves for our Al-bearing $CaCl_2$-type samples appears
497 above both SiO_2 post-stishovite and δ-AlOOH. Note that the K_T curve of Zhang et al. (2021) is in
498 excellent agreement with the K_S values determined for the Reuss bound (isotropic stress) in the
499 same study using Brillouin scattering. The previous study of Buchen et al. (2018) employed a
500 sintered polycrystalline sample compressed in a Ne pressure medium, which was argued to
501 represent the Voigt bound of the material (i.e., isotropic strain conditions) as the grain
502 boundaries of the polycrystalline aggregate were locked together. This hypothesis is consistent
503 with the fact that the K_T values obtained by Buchen et al. (2018) are in agreement with the Voigt
504 bound of K_S calculated from the Brillouin scattering data reported by Zhang et al. (2021),

505 although the two trends still diverge owing to differences in K'_0 (Figure 7). The K_T values
506 predicted by Andrault et al. (2003) and Fisher et al. (2018), on the other hand, deviate more
507 significantly from the trends observed in this study and in Zhang et al. (2021), possibly because
508 of the use of solid pressure media (KBr, NaCl) or no pressure medium at all that can induce non-
509 hydrostatic stress in the sample, even when thermal annealing is performed. This highlights the
510 importance of using highly hydrostatic pressure media such as Ne and He in compressibility and
511 elasticity studies, especially at such high-pressure conditions. For this reason, it is difficult to
512 accurately quantify the individual effect of Al and H substitution on the compressibility of
513 stishovite. If we restrict our comparison to the previous studies of Zhang et al. (2021) and Sano-
514 Furukawa et al. (2009), our results suggest that the bulk modulus behavior along the solid
515 solution between $CaCl_2$-type SiO_2 and AlOOH is not linear, since the K_T values determined for
516 Al5 and Al11 do not plot between those of the two end members. Therefore, we argue that
517 excess molar properties may be non-negligible when modelling the thermodynamic stability and
518 elastic properties of the SiO_2-AlOOH solid solutions with $CaCl_2$-type structure at lower mantle
519 conditions.

520

521 **Acknowledgements**

522 We thank Raphael Njul and Detlef Krauße for their help with the sample preparation and
523 assistance with electron microprobe analyses. We also thank two anonymous reviewers and the
524 technical editor for their constructive comments that helped us to improve the manuscript. We
525 acknowledge DESY (Hamburg, Germany), a member of the Helmholtz Association HGF, for the
526 provision of experimental facilities. Parts of this research were carried out at the Extreme
527 Conditions Beamline P02.2, PETRA-III.

References

Andrault, D., Fiquet, G., Guyot, F., and Hanfland, M. (1998) Pressure-induced Landau-type transition in stishovite. Science, 282, 720–724.

Andrault, D., Angel, R.J., Mosenfelder, J.L., and Le Bihan, T. (2003) Equation of state of stishovite to lower mantle pressures. American Mineralogist, 88, 301–307.

Angel, R.J. (2000) Equations of State. Reviews in Mineralogy and Geochemistry, 41, 35–59.

Angel, R.J., and Finger, L.W. (2011) SINGLE: A program to control single-crystal diffractometers. Journal of Applied Crystallography, 44, 247–251.

Angel, R.J., Gonzalez-Platas, J., and Alvaro, M. (2014) EosFit7c and a Fortran module (library) for equation of state calculations. Zeitschrift fur Kristallographie, 229, 405–419.

Birch, F. (1947) Finite elastic strain of cubic crystals. Physical Review, 71, 809–824.

Boehler, R., and De Hantsetters, K. (2004) New anvil designs in diamond-cells. High Pressure Research, 24, 391–396.

Bolfan-Casanova, N., Andrault, D., Amiguet, E., and Guignot, N. (2009) Equation of state and post-stishovite transformation of Al-bearing silica up to 100 GPa and 3000 K. Physics of the Earth and Planetary Interiors, 174, 70–77.

Buchen, J., Marquardt, H., Schulze, K., Speziale, S., Boffa Ballaran, T., Nishiyama, N., and Hanfland, M. (2018) Equation of State of Polycrystalline Stishovite Across the Tetragonal-Orthorhombic Phase Transition. Journal of Geophysical Research: Solid Earth, 123, 7347–7360.

Carpenter, M.A., Hemley, R.J., and Mao, H. (2000) High-pressure elasticity of stishovite and the P42/mnm - Pnnm phase transition. Journal of Geophysical Research, 105, 807–816.

Carpenter, M.A., Evans, D.M., Schiemer, J.A., Wolf, T., Adelmann, P., Böhmer, A.E., Meingast, C., Dutton, S.E., Mukherjee, P., and Howard, C.J. (2019) Ferroelasticity, anelasticity and magnetoelastic relaxation in Co-doped iron pnictide: Ba(Fe0.957Co0.043)2As2. Journal of Physics Condensed Matter, 31.

Chen, H., Leinenweber, K., Prakapenka, V., Prescher, C., Meng, Y., Bechtel, H., Kunz, M., and Shim, S.H. (2020) Possible H2O storage in the crystal structure of CaSiO3 perovskite. Physics of the Earth and Planetary Interiors, 299.

Eberle, M.A., Grasset, O., and Sotin, C. (2002) A numerical study of the interaction between the mantle wedge, subducting slab, and overriding plate. Physics of the Earth and Planetary Interiors, 134, 191–202.

Fischer, R.A., Campbell, A.J., Chidester, B.A., Reaman, D.M., Thompson, E.C., Pigott, J.S., Prakapenka, V.B., and Smith, J.S. (2018) Equations of state and phase boundary for stishovite and CaCl2-type SiO2. American Mineralogist, 103, 792–802.

Gonzalez-Platas, J., Alvaro, M., Nestola, F., and Angel, R.J. (2016) EosFit7-GUI: A new graphical user interface for equation of state calculations, analyses and teaching. Journal of Applied Crystallography, 49, 1377–1382.

Gréaux, S., Kono, Y., Wang, Y., Yamada, A., Zhou, C., Jing, Z., Inoue, T., Higo, Y., Irifune, T., Sakamoto, N., and others (2016) Sound velocities of aluminum-bearing stishovite in the mantle transition zone. Geophysical Research Letters, 43, 4239–4246.

Hirose, K., Takafuji, N., Sata, N., and Ohishi, Y. (2005) Phase transition and density of subducted MORB crust in the lower mantle. Earth and Planetary Science Letters, 237, 239–251.

572 Hübschle, C.B., Sheldrick, G.M., and Dittrich, B. (2011) ShelXle: A Qt graphical user interface
573 for SHELXL. Journal of Applied Crystallography, 44, 1281–1284.

574 Irifune, T., and Ringwood, A.E. (1993) Phase transformations in subducted oceanic crust and
575 buoyancy relationships at depths of 600-800 km in the mantle. Earth and Planetary Science
576 Letters, 117, 101–110.

577 Ishii, T., Shi, L., Huang, R., Tsujino, N., Druzhbin, D., Myhill, R., Li, Y., Wang, L., Yamamoto,
578 T., Miyajima, N., and others (2016) Generation of pressures over 40 GPa using Kawai-type
579 multi-anvil press with tungsten carbide anvils. Review of Scientific Instruments, 87.

580 Ishii, T., Liu, Z., and Katsura, T. (2019a) A Breakthrough in Pressure Generation by a Kawai-
581 Type Multi-Anvil Apparatus with Tungsten Carbide Anvils. Engineering, 5, 434–440.

582 Ishii, T., Kojitani, H., and Akaogi, M. (2019b) Phase Relations of Harzburgite and MORB up to
583 the Uppermost Lower Mantle Conditions: Precise Comparison With Pyrolite by
584 Multisample Cell High-Pressure Experiments With Implication to Dynamics of Subducted
585 Slabs. Journal of Geophysical Research: Solid Earth, 124, 3491–3507.

586 Ishii, T., Miyajima, N., Criniti, G., Hu, Q., Glazyrin, K., and Katsura, T. (2022) High pressure-
587 temperature phase relations of basaltic crust up to mid-mantle conditions. Earth and
588 Planetary Science Letters, 584, 117472.

589 Jiang, F., Gwanmesia, G.D., Dyuzheva, T.I., and Duffy, T.S. (2009) Elasticity of stishovite and
590 acoustic mode softening under high pressure by Brillouin scattering. Physics of the Earth
591 and Planetary Interiors, 172, 235–240.

592 Kaneshima, S. (2019) Seismic scatterers in the lower mantle near subduction zones. Geophysical
593 Journal International, 218, 1873–1891.

Kaneshima, S., and Helffrich, G. (1999) Dipping low-velocity layer in the mid-lower mantle: Evidence for geochemical heterogeneity. Science, 283, 1888–1891.

Kantor, I., Prakapenka, V., Kantor, A., Dera, P., Kurnosov, A., Sinogeikin, S., Dubrovinskaia, N., and Dubrovinsky, L. (2012) BX90: A new diamond anvil cell design for X-ray diffraction and optical measurements. Review of Scientific Instruments, 83, 125102.

Kingma, K.J., Cohen, R.E., Hemley, R.J., and Mao, H.K. (1995) Transformation of stishovite to a denser phase at lower-mantle pressures. Nature, 374, 243–245.

Kirby, S.H., Stein, S., Okal, E.A., and Rubie, D.C. (1996) Metastable mantle phase transformations and deep earthquakes in subducted oceanic lithosphere. Reviews of Geophysics, 34, 261–306.

Komabayashi, T., Hirose, K., Sata, N., Ohishi, Y., and Dubrovinsky, L.S. (2007) Phase transition in CaSiO3 perovskite. Earth and Planetary Science Letters, 260, 564–569.

Lakshtanov, D.L., Vanpeteghem, C.B., Jackson, J.M., Bass, J.D., Shen, G., Prakapenka, V.B., Litasov, K., and Ohtani, E. (2005) The equation of state of Al,H-bearing SiO 2 stishovite to 58 GPa. Physics and Chemistry of Minerals, 32, 466–470.

Lakshtanov, D.L., Litasov, K.D., Sinogeikin, S. V., Hellwig, H., Li, J., Ohtani, E., and Bass, J.D. (2007a) Effect of Al3+ and H+ on the elastic properties of stishovite. American Mineralogist, 92, 1026–1030.

Lakshtanov, D.L., Sinogeikin, S. V., Litasov, K.D., Prakapenka, V.B., Hellwig, H., Wang, J., Sanches-Valle, C., Perrillat, J.P., Chen, B., Somayazulu, M., and others (2007b) The post-stishovite phase transition in hydrous alumina-bearing SiO 2 in the lower mantle of the earth. Proceedings of the National Academy of Sciences of the United States of America,

104, 13588–13590.

Liermann, H.P., Konôpková, Z., Morgenroth, W., Glazyrin, K., Bednarčik, J., McBride, E.E., Petitgirard, S., Delitz, J.T., Wendt, M., Bican, Y., and others (2015) The Extreme Conditions Beamline P02.2 and the Extreme Conditions Science Infrastructure at PETRA III. Journal of Synchrotron Radiation, 22, 908–924.

Litasov, K.D., and Ohtani, E. (2005) Phase relations in hydrous MORB at 18-28 GPa: Implications for heterogeneity of the lower mantle. Physics of the Earth and Planetary Interiors, 150, 239–263.

Litasov, K.D., Kagi, H., Shatskiy, A., Ohtani, E., Lakshtanov, D.L., Bass, J.D., and Ito, E. (2007) High hydrogen solubility in Al-rich stishovite and water transport in the lower mantle. Earth and Planetary Science Letters, 262, 620–634.

Liu, Z., Nishi, M., Ishii, T., Fei, H., Miyajima, N., Ballaran, T.B., Ohfuji, H., Sakai, T., Wang, L., Shcheka, S., and others (2017) Phase Relations in the System MgSiO3-Al2O3 up to 2300 K at Lower Mantle Pressures. Journal of Geophysical Research: Solid Earth, 122, 7775–7788.

Miller, S.C., and Love, W.F. (1967) Tables of Irreducible Representations of Space Groups and Co-representations of Magnetic Space Groups, 1095 p. Pruett Press.

Nisr, C., Leinenweber, K., Prakapenka, V., Prescher, C., Tkachev, S., and Shim, S.H.D. (2017) Phase transition and equation of state of dense hydrous silica up to 63 GPa. Journal of Geophysical Research: Solid Earth, 122, 6972–6983.

Nisr, C., Chen, H., Leinenweber, K., Chizmeshya, A., Prakapenka, V.B., Prescher, C., Tkachev, S.N., Meng, Y., Liu, Z., and Shim, S.H. (2020) Large H2O solubility in dense silica and its

implications for the interiors of water-rich planets. Proceedings of the National Academy of Sciences of the United States of America, 117, 9747–9754.

Niu, F. (2014) Distinct compositional thin layers at mid-mantle depths beneath northeast China revealed by the USArray. Earth and Planetary Science Letters, 402, 305–312.

Nomura, R., Hirose, K., Sata, N., Ohishi, Y., Suetsugu, D., Bina, C., Inoue, T., Wiens, D., and Jellinek, M. (2010) Precise determination of post-stishovite phase transition boundary and implications for seismic heterogeneities in the mid-lower mantle. Physics of the Earth and Planetary Interiors, 183, 104–109.

Ono, S., Ito, E., and Katsura, T. (2001) Mineralogy of subducted basaltic crust (MORB) from 25 to 37 GPa, and chemical heterogeneity of the lower mantle. Earth and Planetary Science Letters, 190, 57–63.

Ono, S., Suto, T., Hirose, K., Kuwayama, Y., Komabayashi, T., and Kikegawa, T. (2002) Equation of state of Al-bearing stishovite to 40 GPa at 300 K. American Mineralogist, 87, 1486–1489.

Orobengoa, D., Capillas, C., Aroyo, M.I., and Perez-Mato, J.M. (2009) AMPLIMODES: Symmetry-mode analysis on the Bilbao Crystallographic Server. Journal of Applied Crystallography, 42, 820–833.

Paterson, M.S. (1982) The determination of hydroxyl by infrared adsorption in quartz, silicate glasses and similar materials. Bulletin de Mineralogie, 105, 20–29.

Pawley, A.R., McMillan, P.F., and Holloway, J.R. (1993) Hydrogen in stishovite, with implications for mantle water content. Science, 261, 1024–1026.

Petrícek, V., Dušek, M., and Palatinus, L. (2014, January 1) Crystallographic computing system

660 JANA2006: General features. Zeitschrift fur Kristallographie. De Gruyter Oldenbourg.

661 Prescher, C., and Prakapenka, V.B. (2015) DIOPTAS: A program for reduction of two-
662 dimensional X-ray diffraction data and data exploration. High Pressure Research, 35, 223–
663 230.

664 Ricolleau, A., Perrillat, J.P., Fiquet, G., Daniel, I., Matas, J., Addad, A., Menguy, N., Cardon, H.,
665 Mezouar, M., and Guignot, N. (2010) Phase relations and equation of state of a natural
666 MORB: Implications for the density profile of subducted oceanic crust in the Earth's lower
667 mantle. Journal of Geophysical Research: Solid Earth, 115.

668 Salje, E.K. (1991) Phase Transitions in Ferroelastic and Co-elastic Crystals. Phase Transitions in
669 Ferroelastic and Co-elastic Crystals. Cambridge University Press.

670 Sano-Furukawa, A., Kagi, H., Nagai, T., Nakano, S., Fukura, S., Ushijima, D., Iizuka, R.,
671 Ohtahtahtani, E., and Yagi, T. (2009) Change in compressibility of δ-AlOOH and δ-AlOOD
672 at high pressure: A study of isotope effect and hydrogen-bond symmetrization. American
673 Mineralogist, 94, 1255–1261.

674 Sano-Furukawa, A., Hattori, T., Komatsu, K., Kagi, H., Nagai, T., Molaison, J.J., dos Santos,
675 A.M., and Tulk, C.A. (2018) Direct observation of symmetrization of hydrogen bond in δ-
676 AlOOH under mantle conditions using neutron diffraction. Scientific Reports, 8, 1–9.

677 Sheldrick, G.M. (2015a) Crystal structure refinement with SHELXL. Acta Crystallographica
678 Section C: Structural Chemistry, 71, 3–8.

679 ——— (2015b) Foundations and Advances SHELXT-Integrated space-group and crystal-
680 structure determination. Acta Cryst, 71, 3–8.

681 Shen, G., Wang, Y., Dewaele, A., Wu, C., Fratanduono, D.E., Eggert, J., Klotz, S., Dziubek,

682 K.F., Loubeyre, P., Fat'yanov, O. V., and others (2020) Toward an international practical
683 pressure scale: A proposal for an IPPS ruby gauge (IPPS-Ruby2020). High Pressure
684 Research, 1–16.

685 Stixrude, L., Lithgow-Bertelloni, C., Kiefer, B., and Fumagalli, P. (2007) Phase stability and
686 shear softening in CaSi O3 perovskite at high pressure. Physical Review B - Condensed
687 Matter and Materials Physics, 75, 1–10.

688 Thomas, S.M., Koch-Müller, M., Reichart, P., Rhede, D., Thomas, R., Wirth, R., and Matsyuk,
689 S. (2009) IR calibrations for water determination in olivine, r-GeO2, and SiO2 polymorphs.
690 Physics and Chemistry of Minerals, 36, 489–509.

691 Umemoto, K., Kawamura, K., Hirose, K., and Wentzcovitch, R.M. (2016) Post-stishovite
692 transition in hydrous aluminous SiO2. Physics of the Earth and Planetary Interiors, 255, 18–
693 26.

694 Weidner, D.J., Bass, J.D., Ringwood, A.E., and Sinclair, W. (1982) The single-crystal elastic
695 moduli of stishovite. Journal of Geophysical Research, 87, 4740–4746.

696 Zhang, Y., Fu, S., Wang, B., and Lin, J.F. (2021) Elasticity of a Pseudoproper Ferroelastic
697 Transition from Stishovite to Post-Stishovite at High Pressure. Physical Review Letters,
698 126, 25701.

699

Figure Captions

Figure 1. Pressure evolution of the unit-cell volume (**a**) and the unit-cell lattice parameters (**b**,**c**) of samples Al5 and Al11 investigated in this study. Error bars are smaller than the symbols and thus are not shown in the figures. Splitting of the *a* and *b* unit-cell parameters of Al5, indicating the tetragonal to orthorhombic phase transition, is observed at 16.09(2) GPa. Solid black symbols are tetragonal Al5; empty black symbols are orthorhombic Al5; empty red symbols are orthorhombic Al11. Dashed black lines are BM3 fits of tetragonal Al5; solid black lines are BM3 fits of orthorhombic Al5; solid red lines are BM3 fits of orthorhombic Al11.

Figure 2. Comparison of the isothermal bulk moduli of tetragonal Al5 at ambient conditions with isothermal (static compression) and adiabatic bulk moduli (elasticity) from previous studies on SiO_2 and aluminous stishovite. W1982: Weidner et al. (1982), Brillouin scattering (BS) measurements at room pressure. L2007: Lakshtanov et al. (2007a), BS measurements at room pressure. J2009: Jiang et al. (2009), BS measurements in DAC. G2006: Gréaux et al. (2016), ultrasonic interferometry (UI) measurements in large volume press (LVP). Z2021: Zhang et al. (2021), BS measurements at room and high pressure. A2003: Andrault et al. (2003), powder and single crystal XRD in DAC. O2002: Ono et al. (2002), powder XRD in DAC. L2005: Lakshtanov et al. (2005), powder XRD in DAC. B2009: Bolfan-Casanova et al. (2009), powder XRD in DAC. F2018: Fischer et al. (2018), powder XRD in DAC. Z2021: Zhang et al. (2021), single crystal XRD in DAC. Relatively dry Al-bearing samples (G2016, B2009) seem to show a steeper decrease in K_0 with increasing Al content with respect to more H-rich samples (this study, L2007). Note that the solid and dashed line representing the SiO_2-AlOOH and SiO_2-$AlO_{1.5}$ substitution mechanisms are meant to be just a guide to the eye.

Figure 3. Pressure evolution of structural parameters related to the tetragonal-to-orthorhombic phase transition in Al5 stishovite. The inset shows the direction of shortening and lengthening of

724 the unit-cell of post-stishovite, indicated by the spontaneous strains e_1 and e_2 (thick black
725 arrows), as well as the direction of elastic shear softening (thin gray arrows). Green and orange
726 curved arrows indicate the rotation of (Si,Al)O_6 octahedra about the *c*-axis, showing the effect of
727 the Γ2+ distortion. The squared difference of symmetry breaking strains e_1 and e_2 (red squares) is
728 non-zero above 16 GPa, but becomes linear only after 35 GPa, with a predicted transition
729 pressure of 24.7(1.1) GPa (red line). The squared amplitude of the Γ2+ distortion, on the other
730 hand, starts to increase significantly only above 20 GPa. In this case, a linear fit above 35 GPa
731 yields a predicted transition pressure of 24.1(1.9) GPa.

732 **Figure 4**. Pressure evolution of octahedral tilting angles (η) in Al5 (solid circles) and Al11
733 (empty circles). Solid lines represent linear fit to the datapoints between 0 (Al11) or 25 (Al5) and
734 50 GPa. Error bars are not shown as they are smaller than the symbols. η angles are defined by
735 dashed lines superimposed to the crystal structures of stishovite (space group $P4_2/mnm$) and
736 post-stishovite (*Pnnm*) at the right of the graph.

737 **Figure 5**. Linear coupling between the amplitude of the irrep Γ2+ and (a) the symmetry breaking
738 strain; and (b) the octahedral tilting angle. When not shown, errors are smaller than the symbols.

739 **Figure 6**. Stacked Raman spectra of (**a**) Al5 and (**b**) Al11 show the pressure evolution of the soft
740 optic mode B_{1g} (tetragonal symmetry) and the optic mode A_g (orthorhombic symmetry).
741 Pressures marked with an asterisk denote points collected upon decompression. The Raman shift
742 of the B_{1g} and Ag mode of Al5 (**a**) keep decreasing even after Al5 became orthorhombic (~16
743 GPa) up to 20 GPa and remains almost constant between 20 and 30 GPa. Only above this
744 pressure, the Raman shift starts to increase. In the Al11 sample (**b**), splitting of A_g mode occurs
745 above 25 GPa upon compression with the peak at lower wavenumber becoming progressively
746 less intense with increasing pressure. Upon decompression, only small shoulders, but no clear
747 splitting, are observed in the same pressure interval, as shown by spectra collected at 35.50,

30.18 and 25.0 GPa. In (**c**), the squared Raman shifts of the optic modes of Al5 (red circles and solid lines) and Al11 (red squares and dashed line) are plotted against pressure and compared to the same optic mode of SiO_2 (Zhang et al., 2021, empty circles, dashed black lines) and Al,H-bearing stishovite (Lakshtanovet al., 2007b, empty diamonds, dotted black lines). A plateau between 20 and 35 GPa (Al5) and between 0 and 25 GPa (Al11) appears only in our AlOOH-rich compositions. This corroborates our hypothesis that the evolution of the optic mode is not only affected by octahedral tilting, but also by the concentration and bonding of the H atoms.

Figure 7. High-pressure evolution of the isothermal bulk modulus of $CaCl_2$-type pure and Al,H-bearing SiO_2, and AlOOH from this and previous studies. Z2021: Zhang et al. (2021), single-crystal XRD in DAC. A2003: Andrault et al. (2003), powder and single crystal XRD in DAC. F2018: Fischer et al. (2018), powder XRD in DAC. B2018: Buchen et al. (2018), powder XRD in DAC. S2009: Sano-Furukawa et al. (2009), powder XRD in DAC. Labels between brackets show the Al content as Al/(Al+Si). Adiabatic bulk moduli in the Reuss (solid symbols) and Voigt (empty symbols) bounds calculated from single-crystal BS measurements of Zhang et al. (2021) are shown for comparison.

This is the peer-reviewed, final accepted version for American Mineralogist, published by the Mineralogical Society of America.
The published version is subject to change. Cite as Authors (Year) Title. American Mineralogist, in press.
DOI: https://doi.org/10.2138/am-2022-8546. http://www.minsocam.org/

764 **Tables**

765 **Table 1**. 3rd-order Birch-Murnaghan equation of state parameters of tetragonal ($P4_2/mnm$) and
766 orthorhombic (*Pnnm*) Al5 and orthorhombic (*Pnnm*) Al11. Numbers in parentheses represent
767 one standard deviation on the last digits. K'_{T0} of tetragonal Al5 was fixed to the value reported by
768 Zhang et al. (2021) for SiO_2 stishovite. $M'_{c,0}$ of tetragonal Al5 was fixed to 0, while that of
769 orthorhombic Al5 was fixed to the same $M'_{c,0}$ value of Al11.

	Al5		**Al11**
	$P4_2/mnm$	*Pnnm*	*Pnnm*
V_0	47.163(6)	47.44(3)	47.731(7)
K_{T0}	299.3(2.0)	266(4)	280.8(1.3)
K'_{T0}	4.8 (fixed)	4.23(13)	3.89(5)
a_0	4.2006(2)	4.175(2)	4.2546(1)
$M_{a,0}$	659(10)	1357(98)	760(5)
$M'_{a,0}$	28.4(1.8)	20.2(3.7)	30.0(5)
b_0		4.269(6)	4.1843(4)
$M_{b,0}$		327(20)	573(4)
$M'_{b,0}$		14.6(9)	9.73(15)
c_0	2.6734(5)	2.6757(4)	2.6828(2)
$M_{c,0}$	1578(16)	1468(8)	1447(14)
$M'_{c,0}$	0 (fixed)	1.3 (fixed)	1.3(4)

770

771

This is the peer-reviewed, final accepted version for American Mineralogist, published by the Mineralogical Society of America.
The published version is subject to change. Cite as Authors (Year) Title. American Mineralogist, in press.
DOI: https://doi.org/10.2138/am-2022-8546. http://www.minsocam.org/

Figure 1

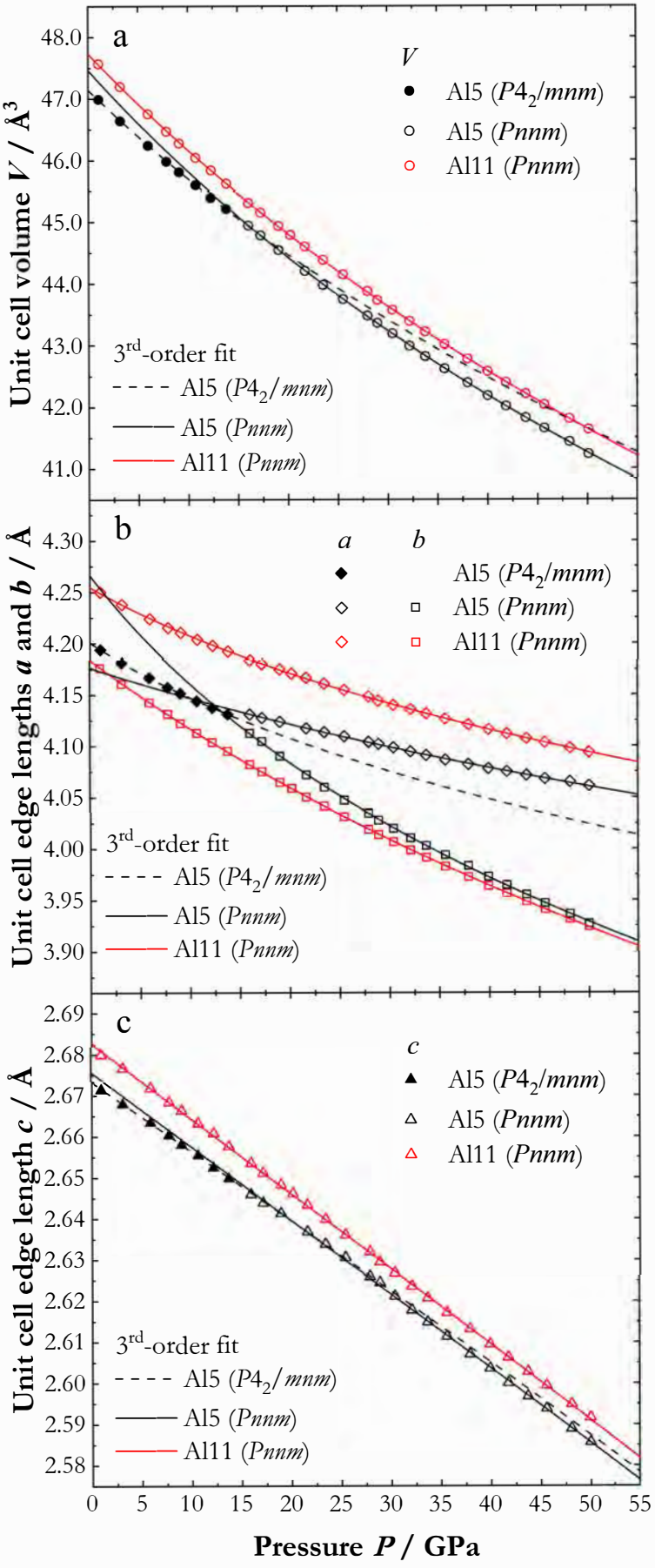

Figure 2

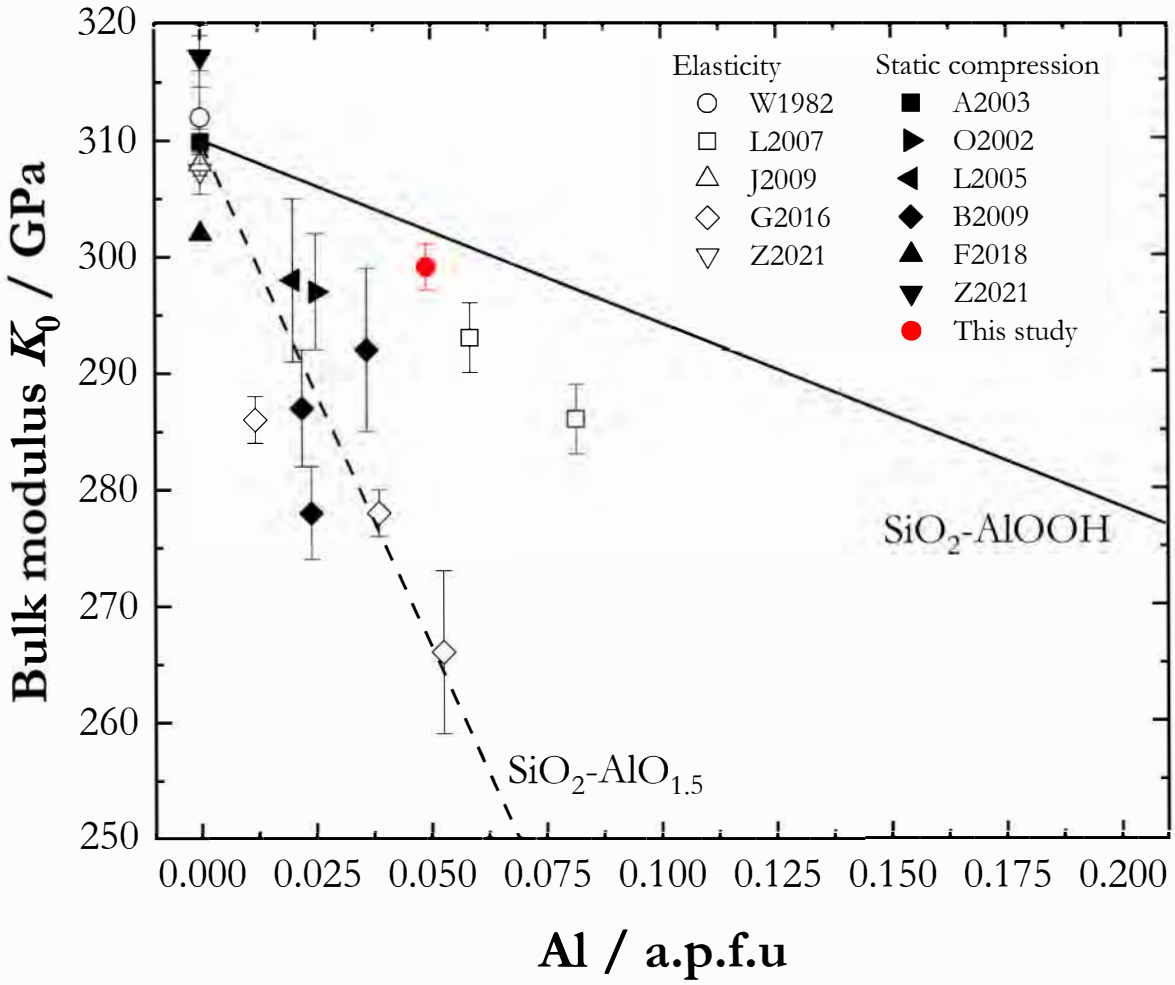

This is the peer-reviewed, final accepted version for American Mineralogist, published by the Mineralogical Society of America.
The published version is subject to change. Cite as Authors (Year) Title. American Mineralogist, in press.
DOI: https://doi.org/10.2138/am-2022-8546. http://www.minsocam.org/

Figure 3

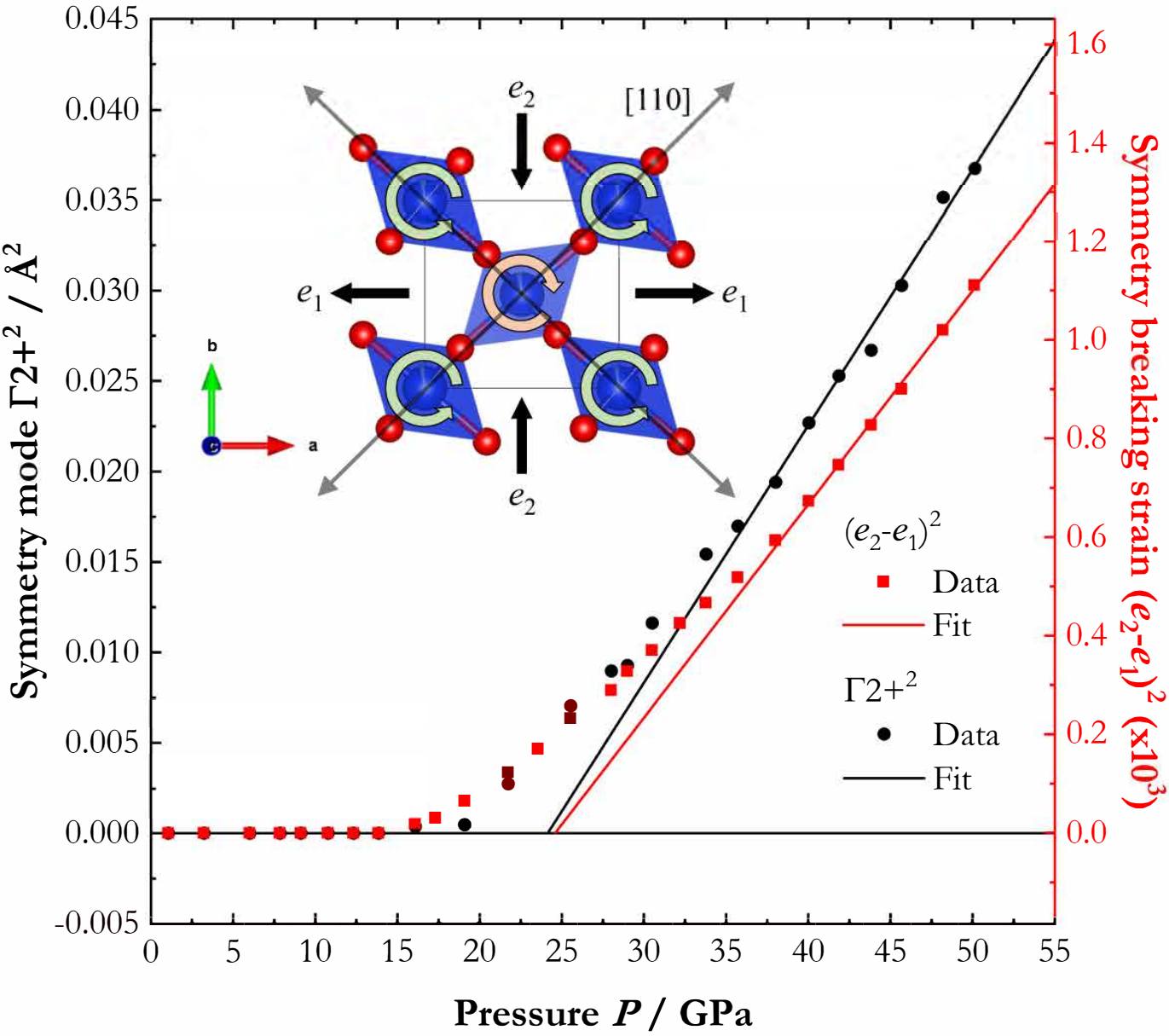

This is the peer-reviewed, final accepted version for American Mineralogist, published by the Mineralogical Society of America.
The published version is subject to change. Cite as Authors (Year) Title. American Mineralogist, in press.
DOI: https://doi.org/10.2138/am-2022-8546. http://www.minsocam.org/

Figure 4

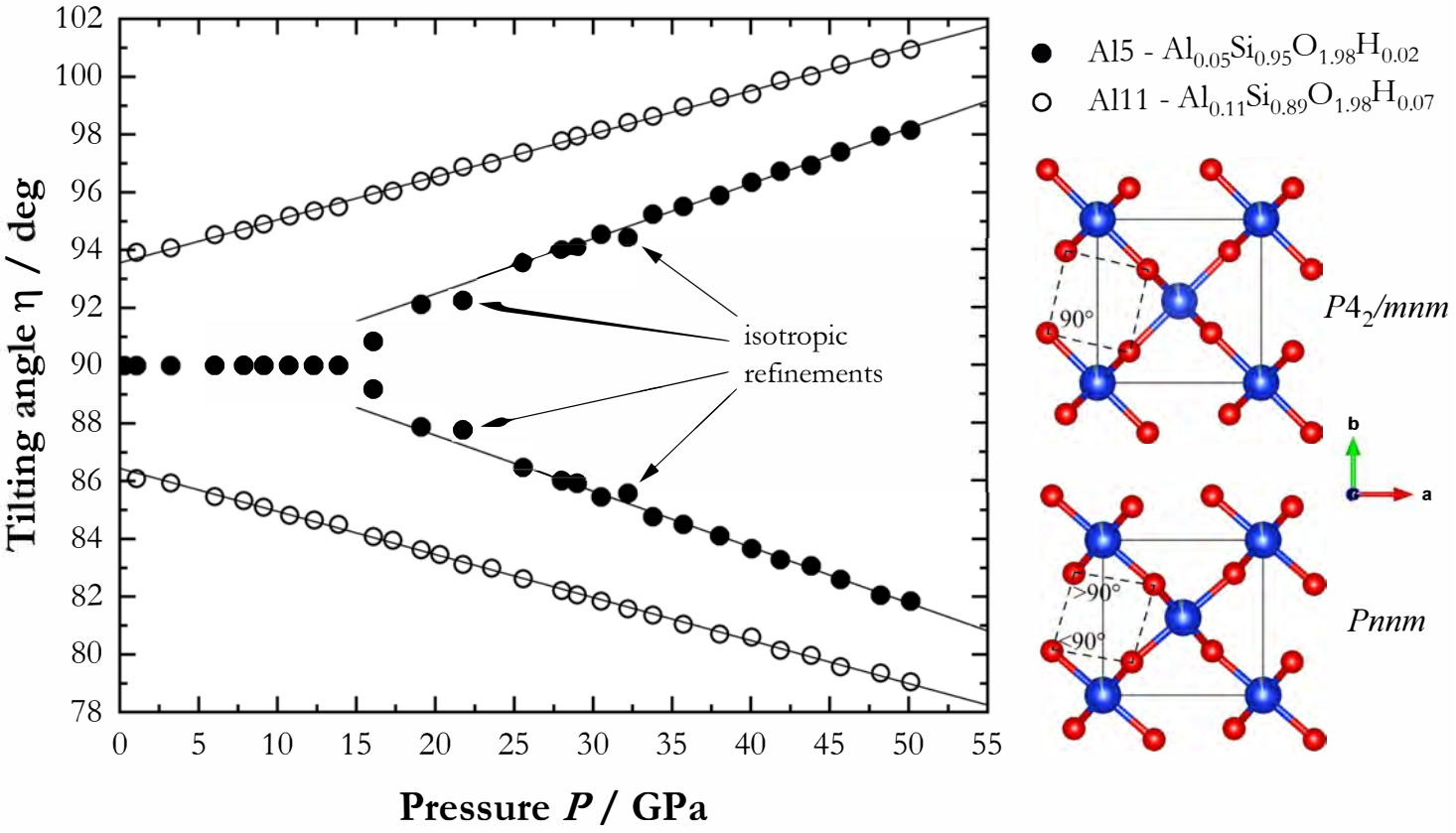

This is the peer-reviewed, final accepted version for American Mineralogist, published by the Mineralogical Society of America.
The published version is subject to change. Cite as Authors (Year) Title. American Mineralogist, in press.
DOI: https://doi.org/10.2138/am-2022-8546. http://www.minsocam.org/

Figure 5

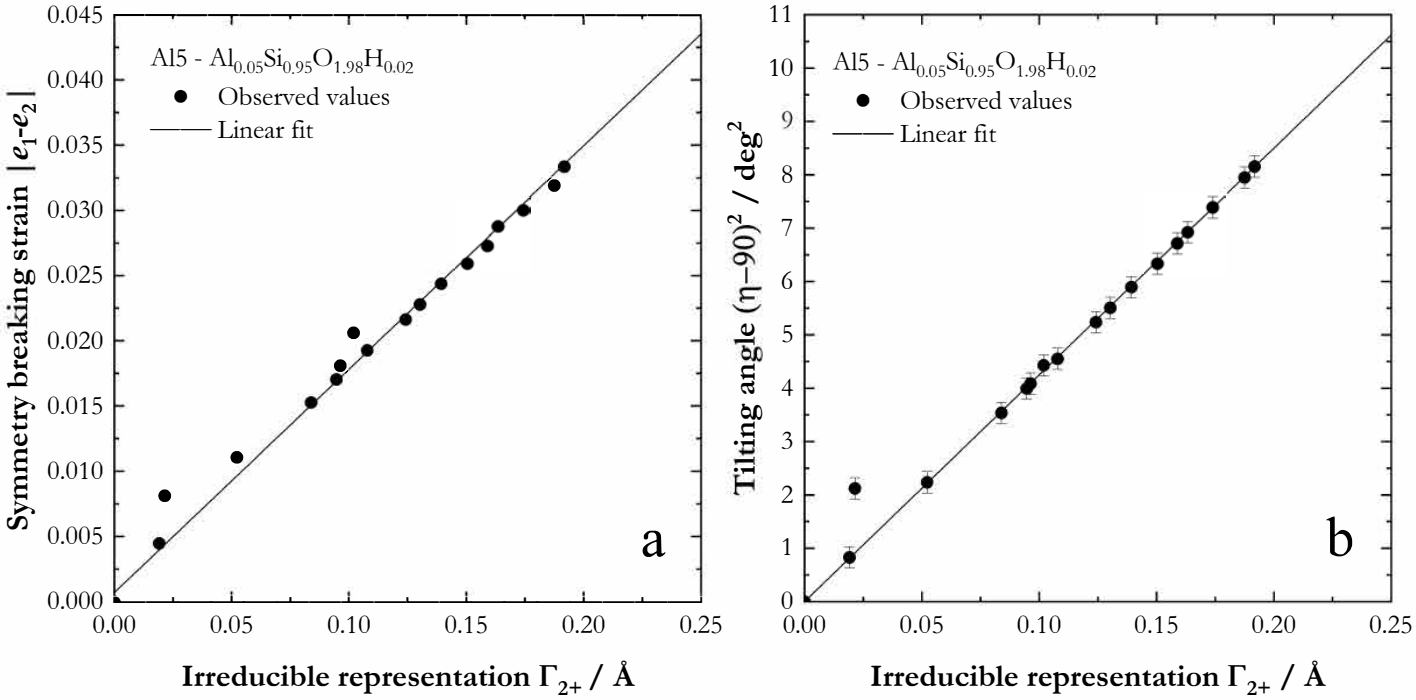

Figure 6

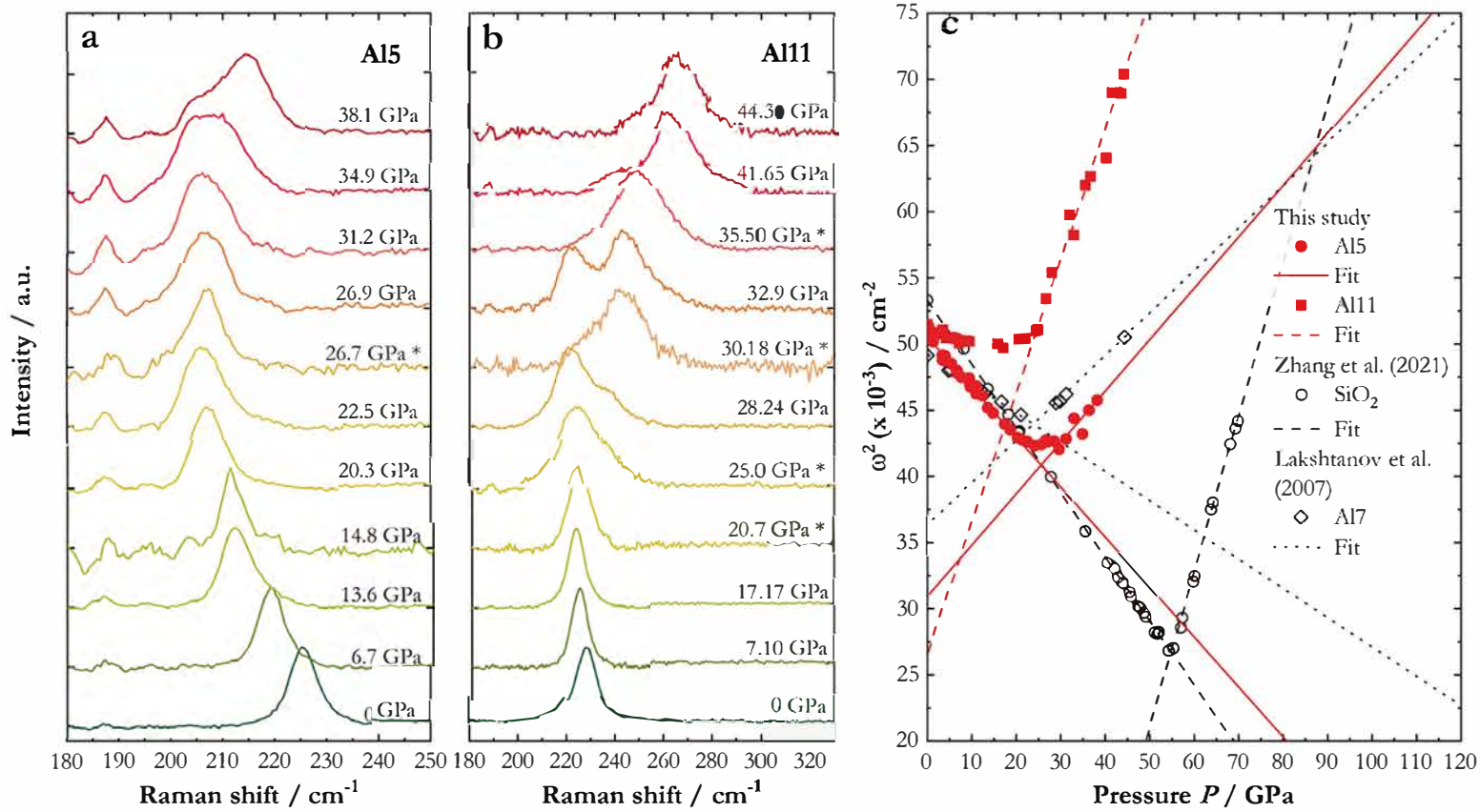

Figure 7